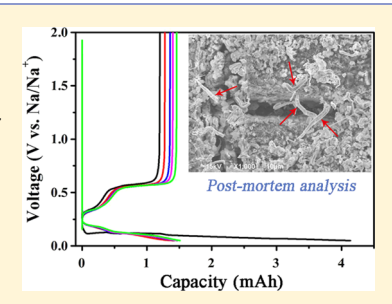
# Damage Formation in Sn Film Anodes of Na-Ion Batteries

Tao Li,<sup>†,‡</sup> Umair Gulzar,<sup>†,‡</sup> Remo Proietti Zaccaria,<sup>†,§</sup> Claudio Capiglia,\*,<sup>†</sup> S. A. Hackney, I and K. E. Aifantis\*, 10

ABSTRACT: Sn anodes for Na-ion batteries exhibit a promising initial capacity of 847 mAh g<sup>-1</sup>, which however, cannot be retained throughout continuous cycling due to the 420% volume changes that Sn experiences during sodiation. Previous experimental studies suggest that fracture does not occur in the submicron Sn particles during the formation of Na-Sn alloys; however, such colossal volume changes must result in microstructural damage. In the present work, the damage mechanisms during sodiation are isolated and accentuated by employing a Sn thick film of 0.5 mm as the anode. This simplified planar geometry allows to dispense with the influence of the binder and carbon additives that are required in porous electrodes. Post-mortem electron microscopy revealed new deformation mechanisms for anode materials, as multiple whiskers nucleated on the



surface of the Sn, whereas pores formed within the Sn (over the Na-ion penetration distance) after electrochemical cycling. These mechanisms were in addition to the dry lake-bed fracture that was also observed. A comparative study on a Sn thin-film anode of 0.06 mm revealed the formation of fracture and pores after cycling, but no whiskers. The whiskers and pores observed in the thick Sn film anode may be more subtle at the nanoscale, and therefore have not been reported for submicron Sn particles in porous electrodes during sodiation.

#### 1. INTRODUCTION

Na-ion batteries (NIBs) are being considered as replacements for Li-ion batteries (LIBs) especially for stationary applications, where the high volumetric and gravimetric energy density of the energy source is not as important as in the automotive and electronic sectors. Stable anodes, however, have not been developed to date, and there exist a few candidates, namely, Sn, Sb, P, and treated forms of carbon. Among these materials, Sn provides a very promising theoretical capacity of 847 mAh g<sup>-1</sup> upon the formation of Na<sub>15</sub>Sn<sub>4</sub>. This capacity, however, cannot be retained during continuous cycling. For example, in the case of microscale Sn particles, a 67% irreversible capacity loss occurs during the first discharge cycle, which has been associated with the 420% volume expansion that occurs upon the formation of Na-Sn alloys. Aiming at mitigating this phenomenon, focus has been given on the fabrication of nanoscale Sn as deformation and fracture are less severe at this scale. In this regard, different kinds of nanostructures, including Sn/C nanocomposites<sup>2–11</sup> and M-Sn intermetallics (M =  $\overline{Cu}$ , Ni, Fe),  $^{12-15}$  have been investigated; however, a capacity over 500 mAh g<sup>-1</sup> for at least 100 cycles was rarely reported. The few exceptions are Sn nanofiber anodes, which gave a charge capacity of 776.26 mAh g<sup>-1</sup> at a rate of 0.1C after 100 cycles,<sup>8</sup> and Sn nanodots encapsulated in porous nitrogen-doped carbon nanofibers (Sn NDs@PNC), which allowed for a reversible capacity of 511 mAh g<sup>-1</sup> at 2000 mA g<sup>-1</sup> for more than 500 cycles.

Of particular interest is the case of Sn/C "pomegranate-like" nanostructured anodes, 4 which gave an initial charge capacity of 503.6 mAh g<sup>-1</sup> with a capacity decay of more than 50% after 100 cycles when cycled against Na. The same anodes allowed for a 88.5% capacity retention (627.9 mAh g<sup>-1</sup>) for 1500 cycles when cycled against Li. This comparison suggests that although Sn also experiences a volume expansion upon lithiation ( $\sim$ 300%), there exist significant differences in the response of Sn between the insertion of Li ions vs Na ions. This is further supported by studies that examine the effects of Li-ion and Na-ion insertion into microstructures. For example, in the case of Li insertion, the Sn particle size in porous electrodes must be below 50 nm to avoid fracture during electrochemical cycling; 16 however, in situ transmission electron microscopy indicated that for the case of Na-ion insertion, Sn particles that were even ~100 nm in diameter did not show any kind of fracture. An ex situ study performed for porous electrodes, which employed Sn/C nanocomposites as the active material, also concluded that after 20 cycles against Na metal, the Sn particles did not experience fracture.<sup>2</sup> The

Received: March 1, 2019 Revised: May 9, 2019 Published: May 22, 2019

15244

<sup>&</sup>lt;sup>†</sup>Istituto Italiano di Tecnologia, via Morego 30, Genova 16163, Italy

<sup>&</sup>lt;sup>‡</sup>DIBRIS, University of Genova, via Opera Pia 13, Genova 16145, Italy

 $<sup>^\</sup>S$ Cixi Institute of Biomedical Engineering, Ningbo Institute of Materials Technology and Engineering, Chinese Academy of Sciences, Ningbo 315201, China

Materials Science and Engineering, Michigan Technological University, Houghton, Michigan 49931, United States

<sup>&</sup>lt;sup>⊥</sup>Mechanical and Aerospace Engineering, University of Florida, Gainesville, Florida 32611, United States

The Journal of Physical Chemistry C

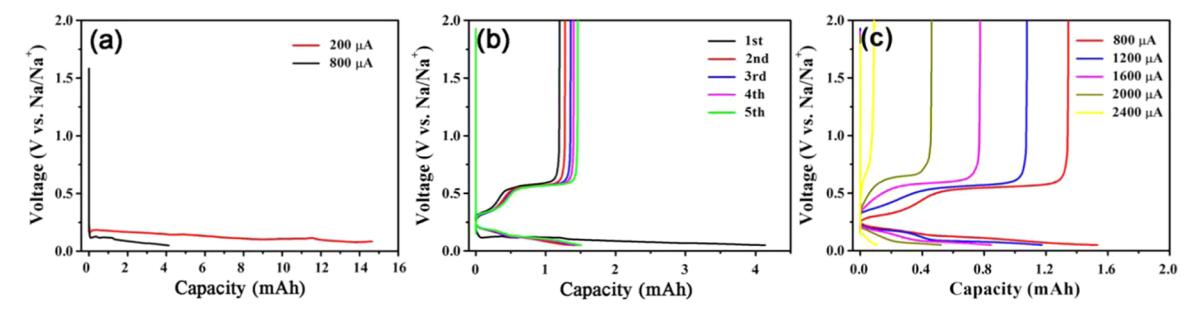


Figure 1. Electrochemical tests of the Na–Sn half cells using a thick Sn foil (0.5 mm in thickness) as the electrode. (a) Initial galvanostatic discharge curves at 200 and 800  $\mu$ A. (b) Galvanostatic charge–discharge curves at 800  $\mu$ A for five cycles. (c) Galvanostatic discharge–charge curves at different currents from 800 to 2400  $\mu$ A.

authors attributed this to the small Sn crystal size, which was measured with X-ray diffraction to be ~90 nm.<sup>2</sup> More recent experiments using in situ hard X-ray nanotomography on Sn porous anodes illustrated fracture in micron-sized Sn particles, during sodiation, but could not detect cracks in Sn particles that were below 500 nm.<sup>17</sup>

The aforementioned differences between sodiation and lithiation of Sn can be interpreted by considering the mechanical behavior of Na-Sn vs Li-Sn. First-principle calculations have shown that the moduli of Sn decrease upon the formation of both Na- and Li-rich alloys. 18,19 Despite this consistent softening in elastic constants, the type of fracture (brittle vs ductile) is approximated by examining the ratio of the bulk modulus with the shear modulus (B/G). Larger values of B/G indicate a more brittle-like behavior, and based on the density functional calculations, it was reported that B/G is higher for Li-Sn alloys, making them more brittle than Na-Sn alloys. 18,19 Furthermore, examination of the phase diagrams for Li-Sn<sup>20</sup> and Na-Sn<sup>21</sup> reveals that the melting points of Na-Sn compounds are substantially lower than the Li-Sn analogues. Therefore, based on the above considerations, a ductile response may be more active upon sodiation of Sn than during its lithiation.

Until now, most of the studies on Sn anodes for NIBs are concerned mainly with the fabrication of Sn-based nanostructures and their electrochemical performance; however, the damage mechanisms that occur during sodiation/desodiation of Sn anodes are rarely reported. The present study, therefore, investigates damage formation in Sn anodes. To do so, Sn foils with different thicknesses (0.5 and 0.06 mm) are employed as the anode since theoretical models and experiments have shown that planar geometries are more prone to mechanical instabilities during ion insertion. <sup>22–25</sup> In addition, this configuration avoids the use of binder and carbon additives that are required in the fabrication of porous electrodes and therefore captures directly the response of Sn to sodiation. The resulting capacities for these anodes are significantly low because of the planar geometry of the electrode, which is not an issue in the present work given the objective of unveiling mechanical damage in Sn and not the realization of a competitive anode for NIBs.

#### 2. EXPERIMENTAL SECTION

**2.1. Electrochemical Tests.** Sn foil (0.5 mm thick) with a purity of 99.998% was purchased from Sigma-Aldrich. The Sn foil was placed in an MBraun glove box under an Ar atmosphere with water and oxygen contents less than 0.1 ppm and was sectioned into 10 mm × 10 mm squares, which

were used as the active electrodes directly without using Al or Cu foil as the current collector. Na metal was employed as the counter and reference electrode, and Whatman fiberglass was used as the separator. The electrolyte solution used was 1.0 M NaClO<sub>4</sub> in propylene carbonate (PC). CR2032-type coin cells were assembled in an Argon-filled glove box. Galvanostatic discharge-charge tests under different currents (800-2400 uA) and cyclic voltammetry (CV) tests at the scanning rate of 0.1 mV s<sup>-1</sup> were conducted over the voltage range of 0.05–2.0 V (vs Na/Na<sup>+</sup>). Electrochemical impedance spectroscopy (EIS) tests were performed in the frequency range from 10 kHz to 0.01 Hz with an alternating voltage amplitude of 5 mV. All electrochemical measurements were carried out using the Biologic BCS-805 multichannel battery test instrument at room temperature. As a comparative study, Sn foils with a smaller thickness of 0.06 mm (purity >99.99%, 8 mm disks, purchased from Sigma-Aldrich) were galvanostatically discharged-charged at current of 500  $\mu$ A in the same voltage range.

**2.2. Characterization.** Scanning electron microscopy (SEM) images were obtained before and after five cycles using a JEOL JEM 6490LA (JEOL, Tokyo, Japan) equipped with a cold FEG, operating at a 15 kV acceleration voltage. The Na—Sn half-cell was disassembled in the Ar-filled glove box, and the Sn electrode was washed with PC and then dried at 70 °C for 3 h. The Sn was then placed in a vial and transferred to the SEM chamber for imaging.

# 3. RESULTS AND DISCUSSION

3.1. Electrochemical Properties. Figure 1a shows the initial galvanostatic discharge curve of the thick Sn foil (0.5 mm in thickness) at currents of 200 and 800  $\mu$ A. For both currents, the Sn electrode exhibits a long sloping plateau below 0.2 V, which can be ascribed to a series of Na-Sn alloying reactions and finally to the formation of Na<sub>15</sub>Sn<sub>4</sub> upon complete sodiation. It should be noted that the capacity measurements are not per gram as the aim of this study is to probe the deformation mechanisms that occur during the sodiation/desodiation, not the anode performance. The discharge capacity at the current of 200 µA is much larger than that of 800  $\mu$ A, demonstrating that a deeper sodiation process occurred in the Sn electrode at a relatively low current. Figure 1b depicts the galvanostatic discharge-charge curves at 800  $\mu$ A for five cycles. In the charge profiles, the Sn electrode exhibited two distinct potential plateaus at ~0.32 and 0.57 V, which are characteristic of stepwise dealloying of Na<sub>15</sub>Sn<sub>4</sub>. The large irreversible capacity loss occurring during the first cycle is associated with the formation of the solid electrolyte interface The Journal of Physical Chemistry C

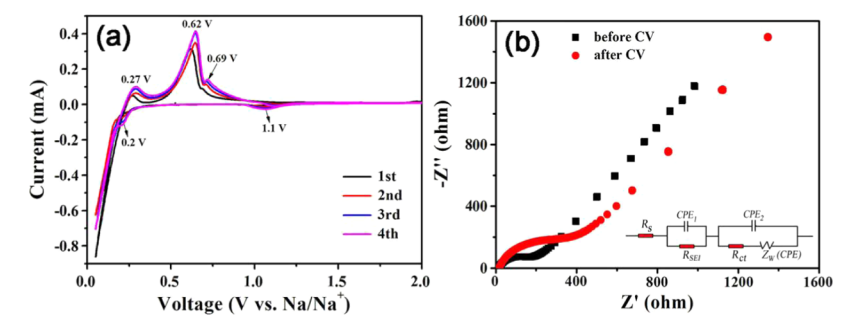


Figure 2. (a) CV profiles of the first four cycles at the scan rate of  $0.1 \text{ mV s}^{-1}$  in the range of  $0.05-2.0 \text{ V vs Na/Na}^+$ . (b) EIS of the Na-Sn half-cell before and after the CV test for four cycles (inset: the equivalent circuit).

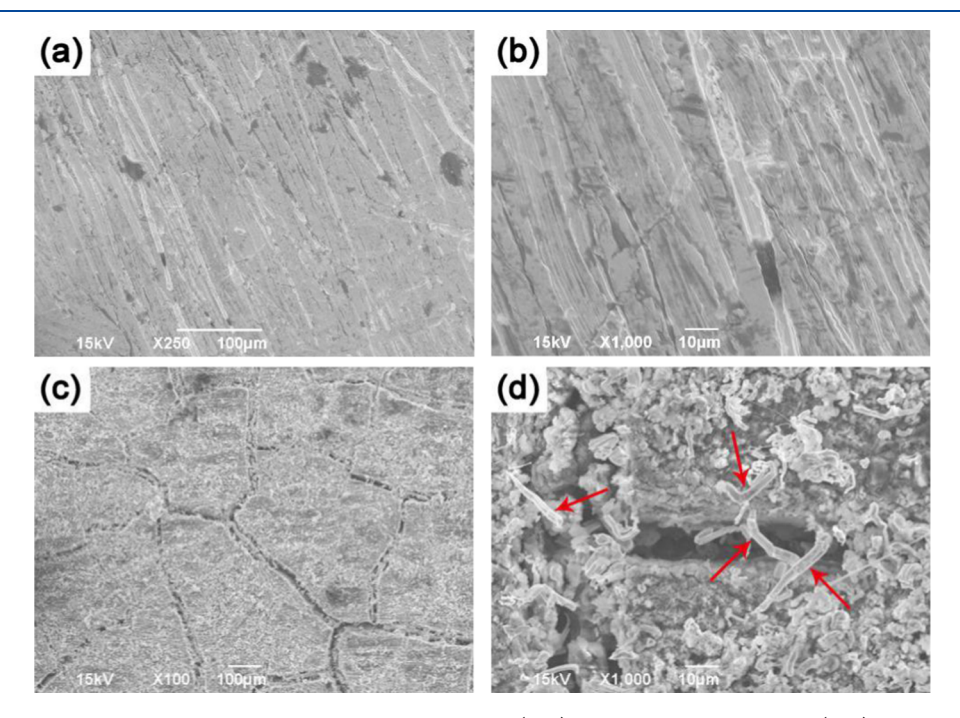


Figure 3. SEM images of surface morphology of the thick Sn foil electrode. (a, b) Sn surface before cycling. (c, d) Sn surface in contact with the electrolyte after five cycles, indicating crack and whisker formation. The red arrows in (d) indicate whisker formation on the fractured particles.

(SEI) layer, as well as to the degradation that Sn experiences due to Na insertion; this will be further elaborated with SEM images in the next section. It is also noted that the discharge/charge capacity increased after the first cycle, which may be due to the structural change after repeated sodiation/desodiation. The Na–Sn half-cell was also tested under different currents from 800 to 2400  $\mu$ A, as shown in Figure 1c. It can be seen that increasing the current resulted in a decrease in the capacity of the Sn electrode due to the increased polarization. The long sloping discharge plateau below 0.2 V is observed even at a high current of 2000  $\mu$ A; however, only a short slope without an obvious plateau is seen when the cell is discharged—charged at a higher current of 2400  $\mu$ A.

Previous studies suggest that during the sodiation process of Sn, four distinguishable plateaus form in a galvanostatic electrochemical profile, corresponding to four different phases. However, for each plateau, with the exception of Na<sub>15</sub>Sn<sub>4</sub>, there are significant debates about the mechanisms giving rise to the alloy formation and their composition and no conclusive results have been reached yet. In the present work, the Sn thick film in the millimeter scale exhibits remarkable differences in the discharge—charge curves when compared to

those previously reported for Sn thin films in the  $\mu$ m scale. <sup>26–29</sup> In this respect, it is very meaningful to investigate Sn anode foils for sodium batteries.

The electrochemical reactivity of pure Sn was also evaluated by CV, as depicted in Figure 2a. During the first cathodic sweep, there is a small reduction peak at 0.2 V and then an intense cathodic current appears at potentials below 0.18 V, corresponding to the Na-Sn alloying process and the formation of highly sodiated phases, i.e., Na<sub>9</sub>Sn<sub>4</sub> and Na<sub>15</sub>Sn<sub>4</sub>. Furthermore, a cathodic peak at a high potential of 1.1 V during subsequent cathodic scans with increasing intensity and potential shifts can be ascribed to the electrolyte decomposition or SEI layer formation. Similar observations have been reported for Sn thick foils and electrodeposited Sn thin-film electrodes for LIBs<sup>32-34</sup> and indicate that the electrolyte reduction processes were not suppressed by the surface film formed on the Sn-foil electrode. The above characteristics of the CV curves can be interpreted by the volume changes that occur during Na+ insertion and deinsertion in the Sn and will be discussed in the next section where SEM images illustrate the surface morphology throughout cycling. In the anodic scans, three well-defined anodic peaks can be identified at ~0.27, 0.62, and 0.69 V,

respectively, corresponding to desodiation from Na<sub>15</sub>Sn<sub>4</sub>, NaSn, and NaSn<sub>5</sub>. These desodiation potentials are in good agreement with the calculated and experimental values for Sn anodes. However, it should be noted that a precise comparison with data in the literature cannot be performed as Sn thick sheets electrodes have not been cycled before.

Finally, EIS of the Na-Sn half-cell before and after the CV tests was also performed to study the detailed interfacial kinetics. As shown in Figure 2b, the Nyquist plots exhibit one depressed semicircle in the high-medium frequency region followed by a sloping line in the low-frequency region. An intercept at the Z'-axis at high frequency indicates the Ohmic resistance  $(R_s)$  of the tested cell. The depressed semicircle at high-medium frequencies is associated with two overlapped interface impedances, i.e., SEI film and charge transfer impedance ( $R_{SEI}$  and  $R_{cv}$  respectively), whereas the inclined line in the low-frequency region stands for the Warburg impedance  $(Z_w)$  corresponding to the sodium diffusion within the bulk of the electrode material.9 The Sn electrode shows a much larger semicircle after four CV cycles, indicating an increase in the interface resistance. To better interpret the EIS data, a typical equivalent circuit model is given as an inset in Figure 2b, where a constant phase element replaces the pure capacitance and the Warburg component for a better fit. The cell exhibits a similar value for  $R_s$  before and after cycling (14.5 and 15.3  $\Omega$ , respectively) but much larger values for  $R_{\text{SEI}}$  and  $R_{ct}$  after cycling (before: 15.8 and 135  $\Omega$ ; after: 38.9 and 396.8  $\Omega$ , respectively). The obvious increase in interface impedance manifests that serious SEI layer formation and damage could occur on the surface of the Sn foil electrode after electrochemical cycling.

**3.2.** Morphological Degradation of Sn during Sodiation. Ex situ SEM images were taken before and after cycling of the Sn to interpret the capacity fade observed in the galvanostatic charge—discharge cycling of the thick Sn foil anode. From Figure 3a,b, it can be seen that the fresh Sn foil is composed of numerous coarse grains and the surface is relatively flat with some tiny grooves. In Figure 3c,d, the Sn surface that was in contact with the electrolyte is shown after five cycles. Severe mechanical deformation is exhibited, which can be distinguished into two types: (i) dry lake-bed fracture and "micro-island" formation, similar to that experienced by Si and SiSn films during lithiation/delithiation, <sup>24,25</sup> which took place throughout the anode; (ii) Sn whiskers (as indicated by representative red arrows) and fine particles on the Sn electrode (Figure 3d).

To verify that the whiskers were composed of Sn, electron dispersive spectroscopy (EDS) was performed on numerous whiskers as those depicted in Figure 3d. A representative EDS spectrum on a whisker is shown in Figure 4, illustrating that Sn was the dominant element present, whereas Na, C, and O were also present at a low concentration since electrochemical cycling had taken place. Although whisker formation has not been observed for Sn films during sodiation, there has been one example reporting it for 500 nm Sn films cycled against Li metal.<sup>37</sup> However, the authors of that study<sup>37</sup> did not perform EDS to verify that those were Sn whiskers and not fibers from the separator.

To better capture the damage evolution within the Sn foil due to Na insertion/extraction, focused ion beam (FIB) was employed to cut a cross section of the surface shown in Figure 3d so as to take a side view, as depicted in Figure 5. The darker region on the top of Figure 5a is the SEI layer, whereas the

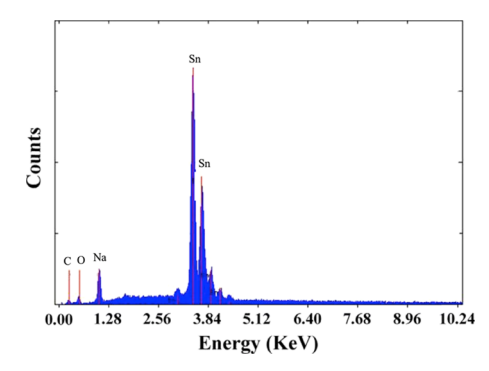


Figure 4. Representative EDS spectrum on whiskers depicted in Figure 3d.

lighter shaded area is the Sn. The SEI formation observed in this anode is more pronounced (and thicker) than in "porous" anodes studied previously. Figure 5a,b reveals that a characteristic effect of Na insertion is pore formation as both large and small pores were observed throughout the cross section. The larger pores were closer to the SEI layer, up to a depth of 3  $\mu$ m, whereas the smaller pores formed deeper into the Sn. This can be due to the fact that sodiation and, hence, volume expansions were more pronounced on the upper surface of the Sn where Na<sup>+</sup> insertion occurred. No pores were observed after a critical depth of approximately  $8-10 \mu m$ . Figure 5c depicts a representative EDS spectrum taken from the darker gray region of Figure 5a, verifying that it is SEI as it is comprised by Na, C, and O, in addition to a small amount of Sn. Figure 5d shows a representative EDS spectrum from inside the pores within the Sn, suggesting that Na is present, as well as traces of O and C. This illustrates that not all Na ions could be fully deinserted.

The severe damage mechanisms and thick SEI layer observed in the Sn foil anode are responsible for the high capacity loss observed in the first cycle shown in Figure 1b, as well as the increase in resistance in the impedance measurements of Figure 2b. Furthermore, the SEI layer was not stable enough to buffer the  $\sim$ 420% volume changes of Sn upon further cycling. Therefore, continuous cycling resulted in the fracture of the SEI, exposing fresh Sn surface to the electrolyte, which resulted in additional SEI to form. Hence, a thick SEI layer developed,  $^{32-34}$  in agreement with the observed cathodic peak at 1.1 V in the CV curves.

3.3. Comparative Study on the Sn Thin Film. The thickness of the Sn film is an important influential parameter of its mechanical and electrochemical behavior upon sodiation/ desodiation; thus, a comparative study on a Sn thin film with a smaller thickness of 0.06 mm (60  $\mu$ m) was carried out. Figure 6a reveals that the thin Sn film displayed similar dischargecharge curves as the thick film of 0.5 mm (Figure 1b) at a similar current. SEM at low magnification (Figure 6b) showed that random cracks (most likely along the grain boundaries) formed on the Sn surface after cycling, which is similar to the dry lake-bed fracture behavior of the thicker film (Figure 3c). A closer observation (Figure 6c) indicates that fine particles and pores formed on the Sn electrode surface; however, no whiskers were observed as in Figure 3d. It is noted that for the 0.06 mm Sn film (Figure 6) the "gaps" between the "microislands" are not as obvious as those that formed in the thick film (Figure 3) but they seem to be filled with deformed Sn structures that connect the surrounding micro-islands. The differences in the mechanical behavior between the thick and

The Journal of Physical Chemistry C

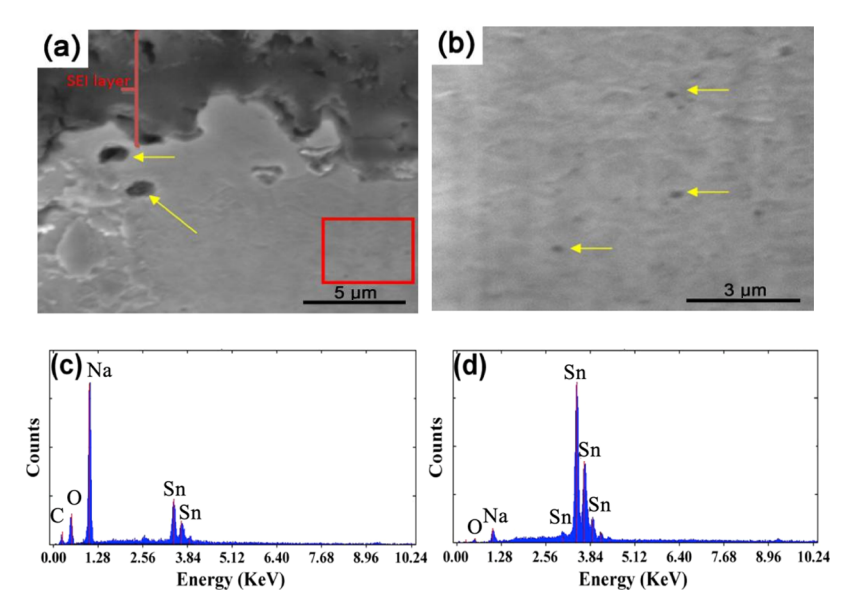
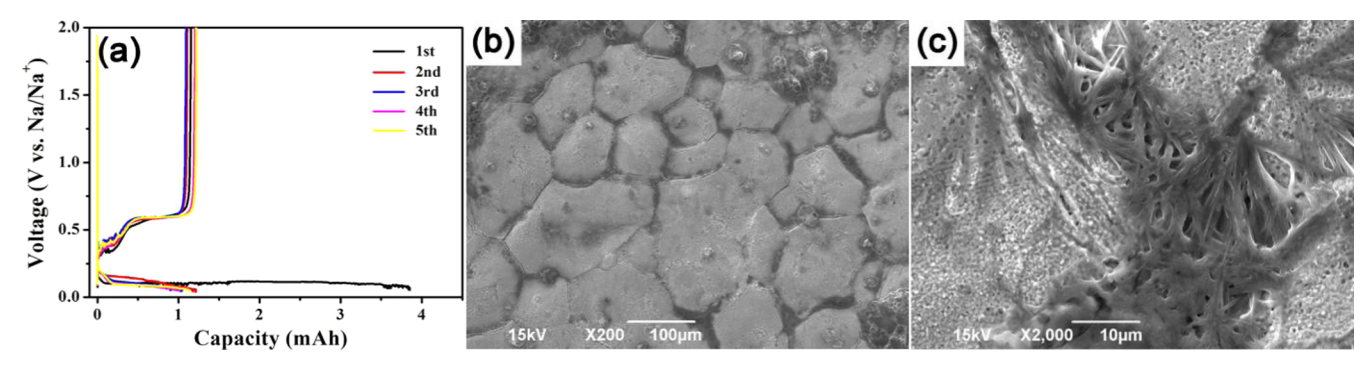


Figure 5. Cross-sectional view obtained with FIB of the Sn surface in contact with the electrolyte. (a) SEI layer appears as dark gray. Micropores are present in the Sn, some of which are indicated by arrows. (b) Magnification of the red square from (a). Multiple nanopores are present, some of which are indicated with arrows. The maximum distance at which these pores were observed was  $\sim$ 8–10  $\mu$ m beneath the interface with the SEI. (c) Representative EDS spectrum from SEI layer of (a). (d) Representative EDS spectrum from within the pores shown in (b).



**Figure 6.** (a) Galvanostatic charge—discharge curves of the thin Sn foil (0.06 mm in thickness) electrode at 500 μA for five cycles. (b, c) SEM images of the Sn foil surface in contact with the electrolyte after five cycles, indicating crack and pore formation.

thin Sn films may be the result from the different stresses that they experience due to their thickness.

3.4. Discussion on the Formation of Pores and Whiskers. Whisker formation in Sn and Sn alloy films is a well-known phenomenon that has plagued the electronics industry for decades.<sup>37</sup> Similarly, pore formation during interdiffusion has been studied extensively beginning in the 1950s.<sup>38</sup> Based on such historical studies concerning these morphological instabilities, whisker formation and porosity development in the Sn planar electrode are expected to be correlated with the development of stresses 39-41 during the sodiation and desodiation processes. According to ref 39, the stress due to a general interdiffusion process is related to both the molar volume change of the alloy with composition and the Kirkendall-effect-induced volume changes. Diffusion-induced pore formation has been considered to result from a combined effect of a Kirkendall-induced tensile stress, excess vacancy concentration, and/or microscopic "cracking of a mud flat on drying"39 similar to that observed in Figure 3c. This sort of tensile stress could develop during desodiation if the Sn selfdiffusion is too slow to accommodate the volume change due to the removal of Na. Whisker growth on the surface of Sn alloys (Figure 3) is known to require a compressive stress 40,41

and is due to a diffusive, coble creep-type mechanism. <sup>41</sup> In this case, the compressive stress during the sodiation process would be the driving force for whisker formation. However, it should be noted that the grain structure may play a role in the whisker growth process and that competing stress relief mechanisms may reduce the prevalence of whisker growth, <sup>41</sup> which explains the lack of whisker formation in the 60  $\mu$ m thin film.

The pore formation observed in both the thin (0.06 mm) and thick (0.5 mm) Sn films was also recently observed on the surface of sodiated Sn films that had a much smaller thickness of 1  $\mu$ m. However, the porosity was significantly more pronounced for the 1  $\mu$ m film than in those studied herein. No other study reports such damage mechanisms during sodiation. However, a closer examination (through magnification) of the SEM images presented in a previous study for Sn microparticles after cycling with respect to Na² does indeed reveal that nanopores formed on the surface of Sn particles. This was not noted by the authors of ref 2 Hence, pore formation does exist at the nanoscale level, but it is less pronounced and has not been highlighted prior to our studies. It should be noted that pore formation has also been noted during deliathion of Sn particles and Si nanowires. Health of the surface of Sn particles and Si nanowires.

Whisker formation has not been observed for micro- and nanoscale Sn particles in porous electrodes; 1,2,16,17 however, from the above postmortem SEM analysis on Sn foils with different thicknesses, we can see that it occurred in the thick Sn film electrode since the mechanically induced stresses caused by Na<sup>+</sup> insertion/deinsertion were accentuated due to the small surface area and large thickness of the Sn film. Whisker formation has also been observed in Sn anodes during cycling against Li and is attributed to the compressive stress along the thickness direction of the film by a "squeeze out" mechanism. 46,47 Whisker formation as a damage mechanism in Sn induces the concern that they could penetrate through the separator and short-circuit the electrochemical cell. Further studies must therefore be performed, examining whisker formation, for porous anodes (with Sn particles as the active material) for NIBs.

#### 4. CONCLUSIONS

Electrochemically cycling of the Sn thick film against Na ions revealed three main damage mechanisms: dry lake-bed fracture, pore formation, and whisker nucleation. This is a unique result, as no other studies have reported the formation of Sn whiskers during sodiation, whereas fracture and pores were noted only in a recent study for Sn thin-film electrodes.<sup>42</sup> As the geometry of the present anodes was planar and the thickness of the Sn film is in the millimeter scale, the damaging effects of sodiation were significantly pronounced, making it possible to observe cracks/pores/whiskers after only five electrochemical cycles. Such pores and whiskers may also form in Sn nanoparticles after long-term cycling. Previous studies do not report pore formation of Sn nanoparticles in porous electrodes during sodiation; however, magnifying published images can reveal such surface asperities. It is therefore important to examine the damage mechanisms in porous electrode that use Sn as the active material during longterm cycling, since if Sn whiskers form, they can penetrate the separator and short-circuit the electrochemical cell, resulting in safety issues. The observation of whiskers and pores suggests ductile fracture of Sn during sodiation despite the large volume expansion that occurs upon the formation of Na-Sn alloys.

### AUTHOR INFORMATION

#### **Corresponding Authors**

\*E-mail: claudio@mvc.biglobe.ne.jp (C.C.).

\*E-mail: kaifantis@ufl.edu (K.E.A.).

ORCID ®

Remo Proietti Zaccaria: 0000-0002-4951-7161

K. E. Aifantis: 0000-0002-8250-918X

**Notes** 

The authors declare no competing financial interest.

## ACKNOWLEDGMENTS

K.E.A. is grateful for the support of the US National Science Foundation CMMI under Grant no. 1762602.

#### REFERENCES

- (1) Wang, J. W.; Liu, X. H.; Mao, S. X.; Huang, J. Y. Microstructural Evolution of Tin Nanoparticles during In Situ Sodium Insertion and Extraction. *Nano Lett.* **2012**, *12*, 5897–5902.
- (2) Datta, M. K.; Epur, R.; Saha, P.; Kadakia, K.; Park, S. K.; Kumta, P. N. Tin and Graphite Based Nanocomposites: Potential Anode for Sodium Ion Batteries. *J. Power Sources* **2013**, 225, 316–322.

- (3) Chen, W.; Deng, D. Carbonized Common Filter Paper Decorated with Sn@C Nanospheres as Additive-Free Electrodes for Sodium-Ion batteries. *Carbon* **2015**, *87*, 70–77.
- (4) Liang, Y.; Tian, H.; Repac, J.; Liou, S.-C.; Chen, J.; Han, W.; Wang, C.; Ehrman, S. Colloidal Spray Pyrolysis: A New Fabrication Technology for Nanostructured Energy Storage Materials. *Energy Storage Mater.* **2018**, *13*, 8–18.
- (5) Ying, H.; Zhang, S.; Meng, Z.; Sun, Z.; Han, W. Ultrasmall Sn Nanodots Embedded inside N-Doped Carbon Microcages as High-Performance Lithium and Sodium Ion Battery Anodes. *J. Mater. Chem. A* **2017**, *5*, 8334–8342.
- (6) Liu, Y.; Zhang, N.; Jiao, L.; Tao, Z.; Chen, J. Ultrasmall Sn Nanoparticles Embedded in Carbon as High-Performance Anode for Sodium-Ion Batteries. *Adv. Funct. Mater.* **2015**, *25*, 214–220.
- (7) Liu, Y.; Xu, Y.; Zhu, Y.; Culver, J. N.; Lundgren, C. A.; Xu, K.; Wang, C. Tin-Coated Viral Nanoforests as Sodium-Ion Battery Anodes. ACS Nano 2013, 7, 3627–3634.
- (8) Nam, D.-H.; Kim, T.-H.; Hong, K.-S.; Kwon, H.-S. Template-Free Electrochemical Synthesis of Sn Nanofibers as High-Performance Anode Materials for Na-Ion Batteries. *ACS Nano* **2014**, *8*, 11824–11835.
- (9) Xie, X.; Kretschmer, K.; Zhang, J.; Sun, B.; Su, D.; Wang, G. Sn@CNT Nanopillars Grown Perpendicularly on Carbon Paper: A Novel Free-Standing Anode for Sodium Ion Batteries. *Nano Energy* **2015**, *13*, 208–217.
- (10) Ruan, B.; Guo, H.-P.; Hou, Y.; Liu, Q.; Deng, Y.; Chen, G.; Chou, S.-L.; Liu, H.-K.; Wang, J.-Z. Carbon-Encapsulated Sn@N-Doped Carbon Nanotubes as Anode Materials for Application in SIBs. ACS Appl. Mater. Interfaces 2017, 9, 37682–37693.
- (11) Liu, Y.; Zhang, N.; Jiao, L.; Chen, J. Tin Nanodots Encapsulated in Porous Nitrogen-Doped Carbon Nanofibers as a Free-Standing Anode for Advanced Sodium-Ion Batteries. *Adv. Mater.* **2015**, 27, 6702–6707.
- (12) Lin, Y.-M.; Abel, P. R.; Gupta, A.; Goodenough, J. B.; Heller, A.; Mullins, C. B. Sn—Cu Nanocomposite Anodes for Rechargeable Sodium-Ion Batteries. ACS Appl. Mater. Interfaces 2013, 5, 8273—
- (13) Kim, I. T.; Allcorn, E.; Manthiram, A. Cu<sub>6</sub>Sn<sub>5</sub>—TiC—C Nanocomposite Anodes for High-Performance Sodium-Ion Batteries. *J. Power Sources* **2015**, 281, 11—17.
- (14) Liu, J.; Wen, Y.; van Aken, P. A.; Maier, J.; Yu, Y. Facile Synthesis of Highly Porous Ni–Sn Intermetallic Microcages with Excellent Electrochemical Performance for Lithium and Sodium Storage. *Nano Lett.* **2014**. *14*. 6387–6392.
- (15) Edison, E.; Satish, R.; Ling, W. C.; Bucher, N.; Aravindan, V.; Madhavi, S. Nanostructured Intermetallic FeSn<sub>2</sub>-Carbonaceous Composites as Highly Stable Anode for Na-Ion Batteries. *J. Power Sources* **2017**, 343, 296–302.
- (16) Aifantis, K. E.; Huang, T.; Hackney, S. A.; Sarakonsri, T.; Yu, A. Capacity Fade in Sn–C Nanopowder Anodes Due to Fracture. *J. Power Sources* **2012**, *197*, 246–252.
- (17) Wang, J.; Eng, C.; Chen-Wiegart, Y. K.; Wang, J. Probing Three-Dimensional Sodiation—Desodiation Equilibrium in Sodium-Ion Batteries by in Situ Hard X-Ray Nanotomography. *Nat. Commun.* **2015**, *6*, No. 7496.
- (18) Mortazavi, M.; Deng, J.; Shenoy, V. B.; Medhekar, N. V. Elastic Softening of Alloy Negative Electrodes for Na-Ion Batteries. *J. Power Sources* **2013**, 225, 207–214.
- (19) Qi, Y.; Hector, L. G., Jr.; James, C.; Kim, K. J. Lithium Concentration Dependent Elastic Properties of Battery Electrode Materials from First Principles Calculations. *J. Electrochem. Soc.* **2014**, *161*, F3010–F3018.
- (20) Sangster, J.; Bale, C. W. The Li-Sn (Lithium-Tin) System. J. Phase Equilib. 1998, 19, 70–75.
- (21) Predel, B. Li-Mg-Nd-Zr. Landolt-Börnstein Group IV Physical Chemistry; Madelung, O., Ed.; Springer: Berlin, Heidelberg, 1997; Vol. 5H, pp 1–4.

- (22) Aifantis, K. E.; Hackney, S. A. Mechanical Stability for Nanostructured Sn- and Si-Based Anodes. *J. Power Sources* **2011**, *196*, 2122–2127.
- (23) Aifantis, K. E.; Dempsey, J. P. Stable Crack Growth in Nanostructured Li-Batteries. *J. Power Sources* **2005**, *143*, 203–211.
- (24) Beaulieu, L. Y.; Eberman, K. W.; Turner, R. T.; Krause, L. J.; Dahn, J. R. Colossal Reversible Volume Changes in Lithium Alloys. *Electrochem. Solid-State Lett.* **2001**, *4*, A137–A140.
- (25) Wang, Y. H.; He, Y.; Xiao, R. J.; Li, H.; Aifantis, K. E.; Huang, X. J. Investigation of Crack Patterns and Cyclic Performance of Ti–Si Nanocomposite Thin Film Anodes for Lithium Ion Batteries. *J. Power Sources* **2012**, 202, 236–245.
- (26) Ellis, L. D.; Hatchard, T. D.; Obrovac, M. N. Reversible Insertion of Sodium in Tin. *J. Electrochem. Soc.* **2012**, *159*, A1801–A1805
- (27) Baggetto, L.; Ganesh, P.; Meisner, R. P.; Unocic, R. R.; Jumas, J.-C.; Bridges, C. A.; Veith, G. M. Characterization of Sodium Ion Electrochemical Reaction with Tin Anodes: Experiment and Theory. *J. Power Sources* **2013**, 234, 48–59.
- (28) Nam, D.-H.; Hong, K.-S.; Lim, S.-J.; Kim, T.-H.; Kwon, H.-S. Electrochemical Properties of Electrodeposited Sn Anodes for Na-Ion Batteries. *J. Phys. Chem. C* **2014**, *118*, 20086–20093.
- (29) Baggetto, L.; Bridges, C. A.; Jumas, J.-C.; Mullins, D. R.; Carroll, K. J.; Meisner, R. A.; Crumlin, E. J.; Liu, X.; Yang, W.; Veith, G. M. The Local Atomic Structure and Chemical Bonding in Sodium Tin Phases. *J. Mater. Chem. A* **2014**, *2*, 18959–18973.
- (30) Chou, C.-Y.; Lee, M.; Hwang, G. S. A Comparative First-Principles Study on Sodiation of Silicon, Germanium, and Tin for Sodium-Ion Batteries. *J. Phys. Chem. C* **2015**, *119*, 14843–14850.
- (31) Stratford, J. M.; Mayo, M.; Allan, P. K.; Pecher, O.; Borkiewicz, O. J.; Wiaderek, K. M.; Chapman, K. W.; Pickard, C. J.; Morris, A. J.; Grey, C. P. Investigating Sodium Storage Mechanisms in Tin Anodes: A Combined Pair Distribution Function Analysis, Density Functional Theory, and Solid-State NMR Approach. *J. Am. Chem. Soc.* **2017**, 139, 7273–7286.
- (32) Li, J.-T.; Chen, S.-R.; Fan, X.-Y.; Huang, L.; Sun, S.-G. Studies of the Interfacial Properties of an Electroplated Sn Thin Film Electrode/Electrolyte Using in Situ MFTIRS and EQCM. *Langmuir* **2007**, 23, 13174–13180.
- (33) Lucas, I. T.; Pollak, E.; Kostecki, R. In Situ AFM Studies of SEI Formation at a Sn Electrode. *Electrochem. Commun.* **2009**, 11, 2157–2160
- (34) Inaba, M.; Uno, T.; Tasaka, A. Irreversible Capacity of Electrodeposited Sn Thin Film Anode. *J. Power Sources* **2005**, *146*, 473–477.
- (35) Chevrier, V. L.; Ceder, G. Challenges for Na-ion Negative Electrodes. *J. Electrochem. Soc.* **2011**, *158*, A1011–A1014.
- (36) Xu, Y.; Zhu, Y.; Liu, Y.; Wang, C. Electrochemical Performance of Porous Carbon/Tin Composite Anodes for Sodium-Ion and Lithium-Ion Batteries. *Adv. Energy Mater.* **2013**, *3*, 128–133.
- (37) Furuta, N.; Hamamura, K. Growth mechanism of proper tin-whisker. *Jpn. J. Appl. Phys.* **1969**, *8*, 1404–1410.
- (38) Seitz, F. On the porosity observed in the Kirkendall effect. *Acta Metall.* **1953**, *1*, 355–369.
- (39) Brinkmanf, J. A. Mechanism of pore formation associated with the kindendall effect. *Acta Metall.* **1955**, *3*, 140–145.
- (40) Fisher, R. M.; Darken, L. S.; Carroll, K. G. Accelerated growth of tin whiskers. *Acta Metall.* **1954**, *2*, 368–373.
- (41) Boettinger, W. J.; Johnson, C. E.; Bendersky, L. A.; Moon, K. W.; Williams, M. E.; Stafford, G. R. Whisker and Hillock formation on Sn, Sn—Cu and Sn—Pb electrodeposits. *Acta Mater.* **2005**, *53*, 5033—5050.
- (42) Li, T.; Gulzar, U.; Bai, X.; Lenocini, M.; Prato, M.; Aifantis, K. E.; Capiglia, C.; Zaccaria, R. P. Insight on the Failure Mechanism of Sn Electrodes for Sodium-Ion Batteries: Evidence of Pore Formation during Sodiation and Crack Formation during Desodiation. *ACS Appl. Energy Mater.* **2019**, *2*, 860–866.
- (43) Chao, S.-C.; Yen, Y.-C.; Song, Y.-F.; Chen, Y.-M.; Wu, H.-C.; Wu, N.-L. A Study on the Interior Microstructures of Working Sn

- Particle Electrode of Li-Ion Batteries by in Situ X-Ray Transmission Microscopy. *Electrochem. Commun.* **2010**, *12*, 234–237.
- (44) Lu, X.; Bogart, T. D.; Gu, M.; Wang, C.; Korgel, B. A. In Situ TEM Observations of Sn-Containing Silicon Nanowires Undergoing Reversible Pore Formation Due to Fast Lithiation/Delithiation Kinetics. *J. Phys. Chem. C* 2015, *119*, 21889–21895.
- (45) Choi, J. W.; McDonough, J.; Jeong, S.; Yoo, J. S.; Chan, C. K.; Cui, Y. Stepwise Nanopore Evolution in One-Dimensional Nanostructures. *Nano Lett.* **2010**, *10*, 1409–1413.
- (46) Sobiech, M.; Wohlschlogel, M.; Welzel, U.; Mittemeijer, E. J.; Hugel, W.; Seekamp, A.; Liu, W.; Ice, G. E. Local, Submicron, Strain Gradients as the Cause of Sn Whisker Growth. *Appl. Phys. Lett.* **2009**, 94, No. 221901.
- (47) Li, J.; Yang, F.; Ye, J.; Cheng, Y.-T. Whisker Formation on a Thin Film Tin Lithium-Ion Battery Anode. *J. Power Sources* **2011**, 196, 1474–1477.